Ocean Engineering 238 (2021) 109762

Contents lists available at ScienceDirect

Ocean Engineering

journal homepage: www.elsevier.com/locate/oceaneng

The impacts of internal solitary waves on a submerged floating tunnel

P.X. Zou [a,b,c], Jeremy D. Bricker [a,d,*], Wim.S.J. Uijttewaal [a]

[a] Dept. of Hydraulic Engineering, Faculty of Civil Engineering & Geosciences, Delft University of Technology, 2600, Delft, GA, the Netherlands
[b] CCCC FHDI Engineering Co, Ltd., Guangzhou, Guangdong, 510230, China
[c] CCCC SFT Technical Joint Research Team, Zhuhai, Guangdong, 519080, China
[d] Dept. of Civil and Environmental Engineering, University of Michigan, Ann Arbor, MI, 48109, USA

ARTICLE INFO

Keywords:
Internal solitary wave
Submerged floating tunnel
CFD
Dynamic response
Fluid-structure interaction

ABSTRACT

The interaction between an oceanic internal solitary wave (ISW) and a prototype submerged floating tunnel (SFT) is numerically investigated. Effect of oceanic internal solitary wave amplitude, the relative distance of the SFT to the pycnocline, cross-sectional geometry of the SFT, and the density ratio of the two fluid layers are analyzed. At a potential application site, the dynamic response of an SFT composed of a tube-joint-mooring system forced by an oceanic ISW is studied using Finite Element Method (FEM) modeling. The numerical results show that the ISW-induced force can be effectively reduced by adopting a parametric SFT cross section instead of a circle or ellipse. The influence of the relative distance of the SFT to the ISW pycnocline is crucial, and can remarkably alter the vertical force and buoyancy-weight ratio (BWR) of the SFT during ISW propagation. Large shear forces and bending moments on the SFT can occur, affecting the tension in the mooring lines, and threatening the safety and reliability of the SFT system. However, the deflections and accelerations of the SFT under the applied ISW are within structural serviceability requirements due to the low frequency of the ISW compared to the natural frequency of the SFT tube.

1. Introduction

Internal waves have been confirmed by satellite images and in situ observations as ubiquitous in oceanic environments (Vázquez et al., 2008), (Klymak et al., 2006). The mechanism of internal waves generation is generally as a result of stratified flows over topographic variations such as sills, ridges, and continental shelf edges, corresponding to an energy conversion from barotropic tide into baroclinic internal wave (Ramirez and Renouard, 1998), (Hibiya, 1986). Internal solitary waves (ISWs), associated with non-linear characteristics, are representative of internal waves. ISW's have been recorded with amplitude over 170 m (Klymak et al., 2006), and have been observed to penetrate the entire water depth. These ISWs can induce large wave forcing and hence cause severe hazards to the operation and maintenance of marine engineering structures.

A moored submerged floating tunnel (SFT), as a novel sea-crossing infrastructure suspended under water, is subject to the impacts of hydrodynamic loads induced by ISWs. Therefore, if an SFT is built in regions active with ISW's, it is imperative to analyze the characteristics of interaction between ISWs and the SFT tube body. The SFT tube can be regarded as a cylindrical structure, which is a common component of marine engineering structures. Previous studies of the ISW's effect on cylinders have been carried out using numerous approaches. Ermanyuk and Gavrilov (2005) experimentally investigated the interaction of a small-amplitude internal solitary wave and a horizontal circular cylinder in a two-layer miscible fluid system, and analyzed the effects of the pycnocline thickness and distance between the cylinder and pycnocline on the hydrodynamic loading on the cylinder. (Wang et al. (2018)) carried out an experimental study on the ISW-induced forces acting on a cylinder and explored the effect of splitter plates on force reduction using numerical simulations. Cui et al. (2019) experimentally studied the motion and mooring force of a floating model under ISW impact, and found that the ISW amplitude and the model size are crucial factors affecting the structural response. Ding et al. (2020) investigated the hydrodynamic forces exerted by ISWs on extended and tandem cylinders using OpenFOAM and verified their results against experimental data. However, due to the limitations of these small-scale laboratory tests and simple SFT cross-sectional shapes considered, the characteristics of interaction between ISWs and an SFT under realistic oceanic conditions cannot be properly assessed by the experimental and numerical studies

* Corresponding author. Dept. of Hydraulic Engineering, Faculty of Civil Engineering & Geosciences, Delft University of Technology, 2600, Delft, GA, the Netherlands.
E-mail address: j.d.bricker@tudelft.nl (J.D. Bricker).

https://doi.org/10.1016/j.oceaneng.2021.109762
Received 26 May 2021; Received in revised form 30 July 2021; Accepted 28 August 2021
Available online 4 September 2021

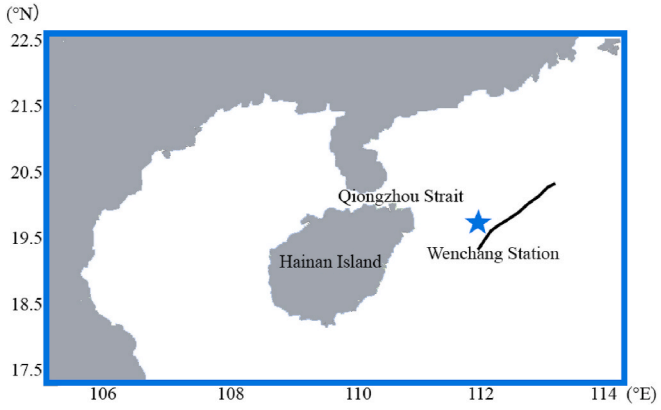

Fig. 1. The locations of Wenchang station and the Qiongzhou Strait. The blue star denotes Wenchang observation station. The black line indicates the sketch of the leading solitary wave. (For interpretation of the references to colour in this figure legend, the reader is referred to the Web version of this article.)

completed thus far.

Empirical methods for ISW-induced load estimation mainly applies the Morison equation. Si et al. (2012) adopted the Morison equation to compute the shear forces and torques induced by ISWs on a rigid cylindrical pile under continuously stratified ocean conditions in the South China Sea. Cai et al. (2003, 2006, 2008)and used the Morison equation, modal separation, and linear regression analysis to estimate the forces and torques resulting from ISWs with and without shear flow on vertical cylindrical piles, and proposed a simple ISW-induced force prediction method based on the dominant term of the global force. Lin and Zan (2021) discussed the influence of adopting local or global empirical parameters on the predictability of the ISW force on a cylinder using the Morison Equation, and concluded that the contribution of the nonlinear term is significant. However, the resulting modified coefficients in the Morison formula are not universal, but vary with the adopted ISW theory and model settings.

Research on the impacts of ISWs on other marine engineering structures is extensive. Song et al. (2011) established an analytical model to compute the forces and response motion of a spar platform under ISWs where the drag and inertial forces are computed by the Morison equation. Lü et al. (2016) studied the impacts of a parabolic background current on force and torque exerted by ISWs on the tendon legs of a tension leg platform using the Morison equation. Chen et al. (2017, 2020) experimentally measured the forces and pitch moments exerted by ISWs on a semi-submersible model to obtain empirical coefficients based on the Morison equation, and examined various wave propagation directions, concluding that the inline and transverse forces are affected significantly by ISWs direction. However, most previous studies focused on vertical cylindrical offshore structures with comparatively small diameters, such as vertical piles or tendon legs. Investigations of ISW impacts on a large-diameter horizontal cylinder such as an SFT are lacking. Moreover, due to the specific structural characteristics of an SFT, its buoyancy-weight ratio (BWR) has a dominant effect on its mooring tension and dynamic response, which influences the serviceability and reliability of the coupled SFT system. The internal wave can directly change the structural buoyancy, and hence, change the BWR. Most previous research on ISW's and marine

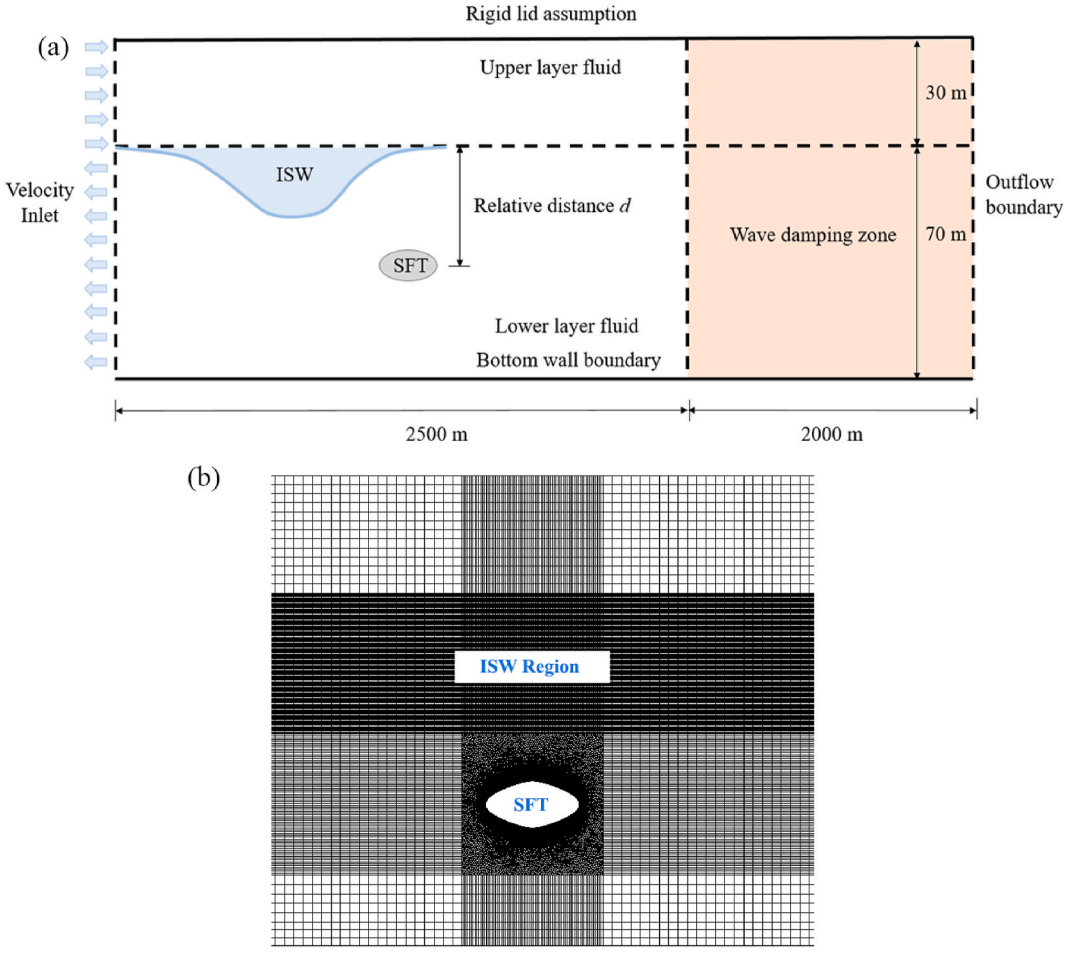

Fig. 2. Model sketch. (a) Computational domain; (b) Local grid settings in different regions.

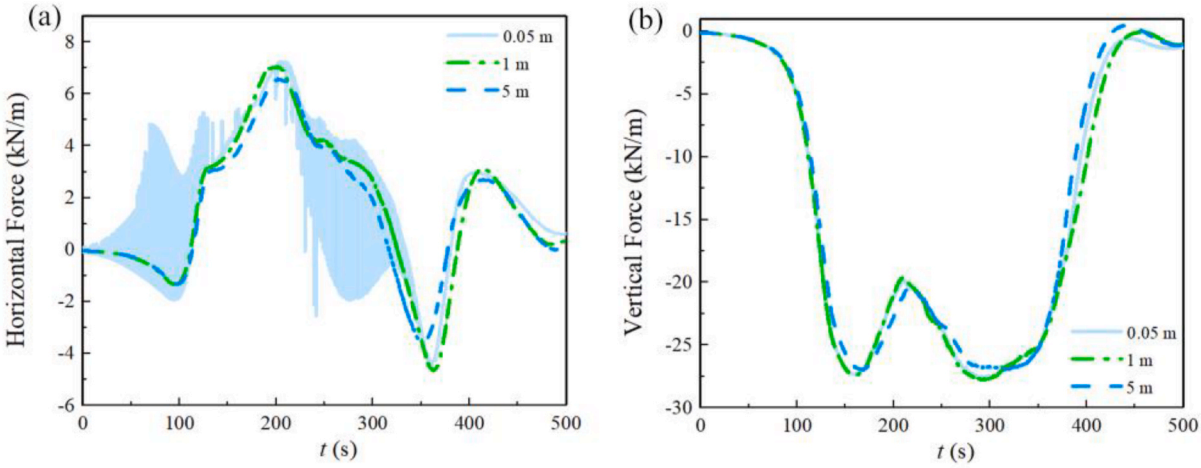

Fig. 3. Sensitivity of force per meter to pycnocline layer thickness. (a) Horizontal unit force on the SFT; (b) vertical unit force on the SFT.

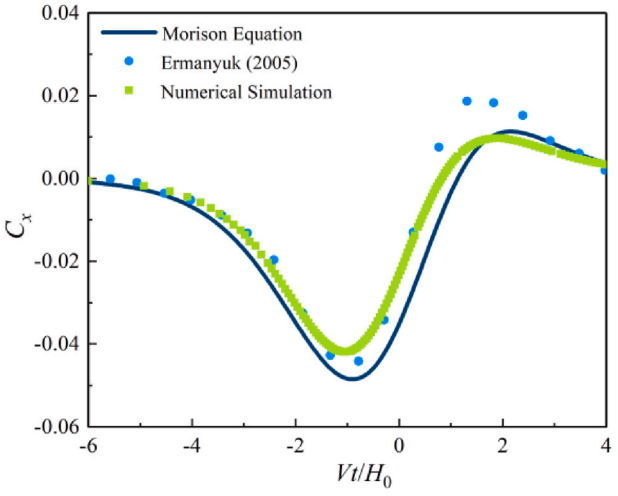

Fig. 4. Comparison of horizontal force coefficients among the Morison Equation, experimental data, and numerical simulation.

engineering structures focused either on the detailed turbulent flow forces induced by the ISW, or on the structural response, but combining turbulent flow simulation with structural dynamic response analysis in a systematic assessment had not yet been accomplished.

To eliminate the scale effect, this present paper studies a full-scale prototype SFT subjected to oceanic ISW. Characteristics of the detailed ISW-SFT interaction during ISW evolution are revealed using Computational Fluid Dynamics (CFD). Dynamic response analysis for a coupled tube-joint-mooring system is then carried out to analyze the ISW impacts on the SFT. The paper is structured as follows. The applied ISW theory and oceanic ISW properties are described in Section 2. Section 3 introduces the model set-up and numerical validation. Section 4 quantifies the influence of the ISW amplitude, the SFT cross-sectional shape, the distance from the SFT to the pycnocline, and the fluid density ratio, on the ISW-SFT interaction. The dynamic response of the SFT in oceanic ISW conditions is analyzed, and the effects of BWR change on the structural internal forcing are discussed in Section 5.

2. Methodology

2.1. ISW wave theory

At present, there are several wave theories that can be applied to describe the shape of an ISW. The Korteweg de Vries (KdV) theory,

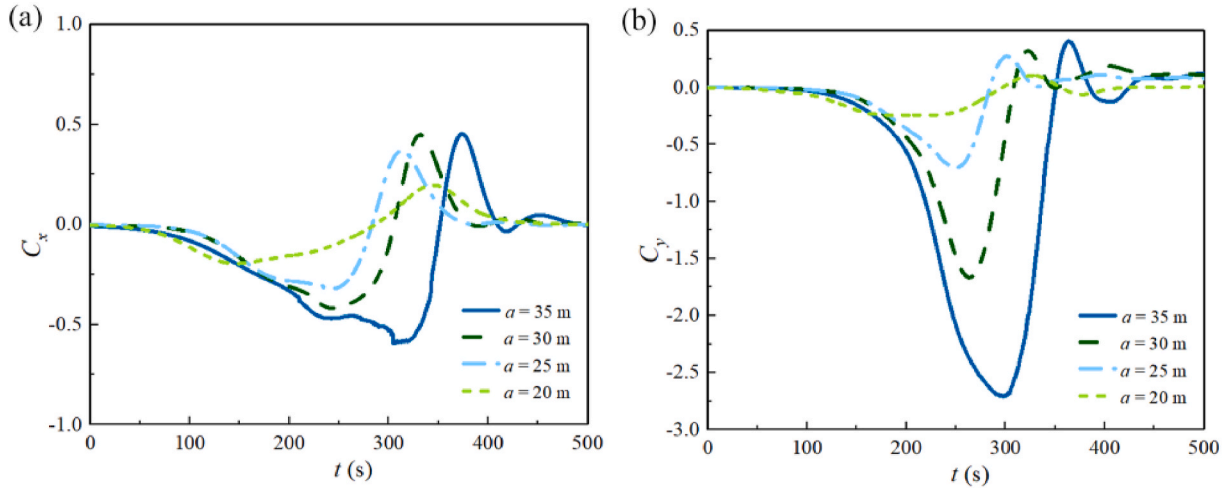

Fig. 5. Time series of force coefficients on the SFT for different ISW amplitudes. (a) Horizontal force coefficient (positive direction is ISW propagation direction); (b) vertical force coefficient (positive direction is upward).

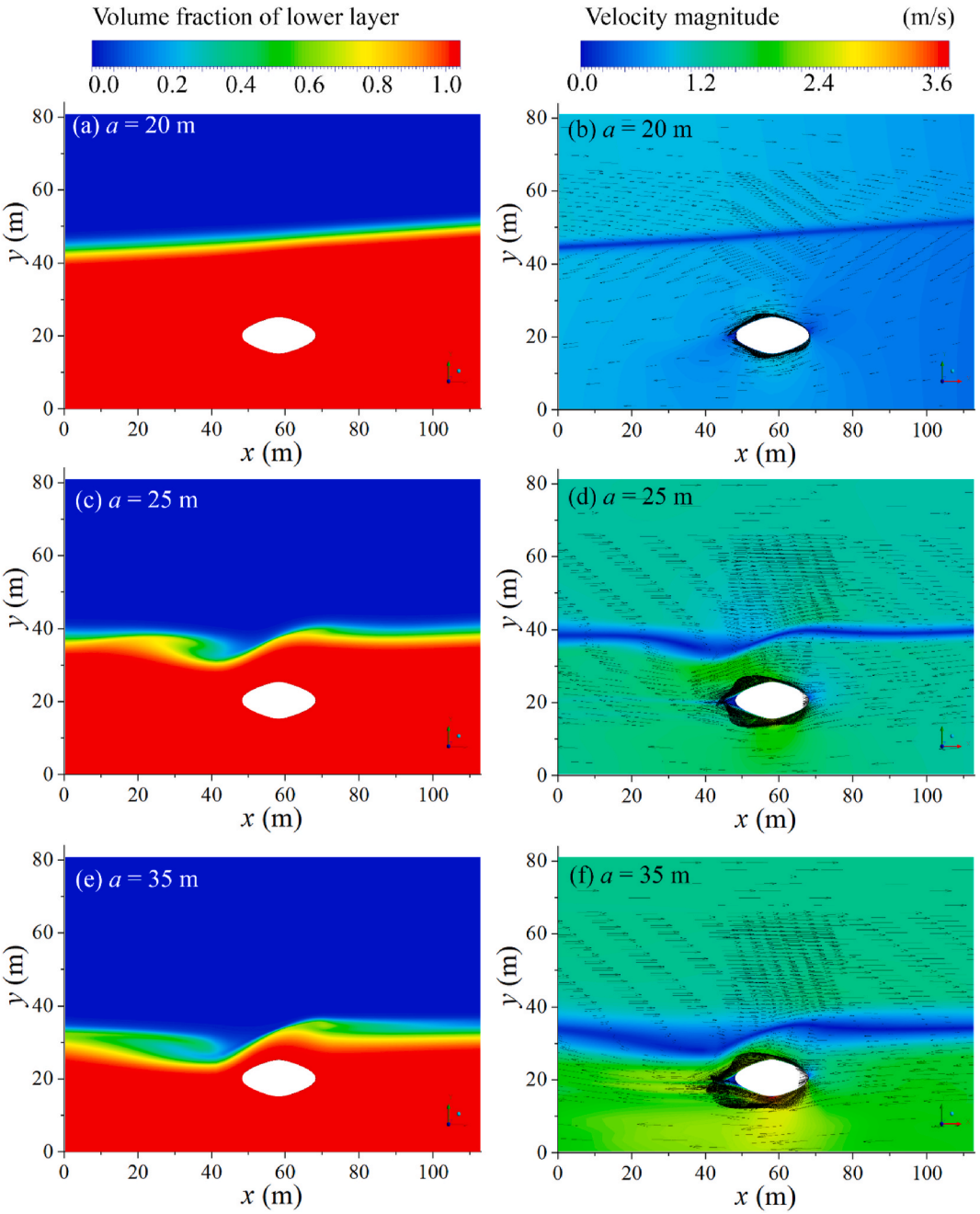

Fig. 6. vol fraction and velocity field around the SFT for different ISW amplitudes. The ISW amplitudes from top to bottom are 20 m, 25 m, and 35 m, respectively.

formulated by Diederic Korteweg and Gustav de Vires, can be adopted to analytically define the internal wave profile. This theory is only suitable for small-amplitude and weakly nonlinear and dispersive waves (Koop and Butler, 1981). By increasing its nonlinearity, an extended KdV (eKdV) (Kakutani and Yamasaki, 1978) wave theory containing both quadratic and cubic nonlinear terms can be applied. Moreover, a modified KdV theory (mKdV) is formulated for large-amplitude internal waves (Michallet and Barthélémy, 1998). The interface displacement governed by the mKdV theory is expressed by Eq. (1)

$$\zeta(x,t)=\frac{a\mathrm{sech}^2[\kappa(x-c_{mKdV}t)]}{1-\mu\tanh^2[\kappa(x-c_{mKdV}t)]} \tag{1}$$

where a is the internal wave amplitude; c_{mKdV} is the phase velocity, and μ and κ are fluid thickness coefficients, given by

$$c_{mKdV}=c_m+B\left[\left(\alpha a+\beta\overline{h}\right)^2-\left(\beta^2-\alpha\right)\overline{h}^2\right] \tag{2}$$

$$\mu=\begin{cases} h''\Big/h' \, if \, \overline{h}>0 \\ h'\Big/'' \, if \, \overline{h}<0 \end{cases} \tag{3}$$

$$\kappa=\left(-\frac{B}{A}h'h''\right)^{0.5} \tag{4}$$

with

$$c_m^2=\frac{gH}{2}\left[1-\sqrt{1-\frac{4h_1h_2(1-\rho_1/\rho_2)}{H^2}}\right] \tag{5}$$

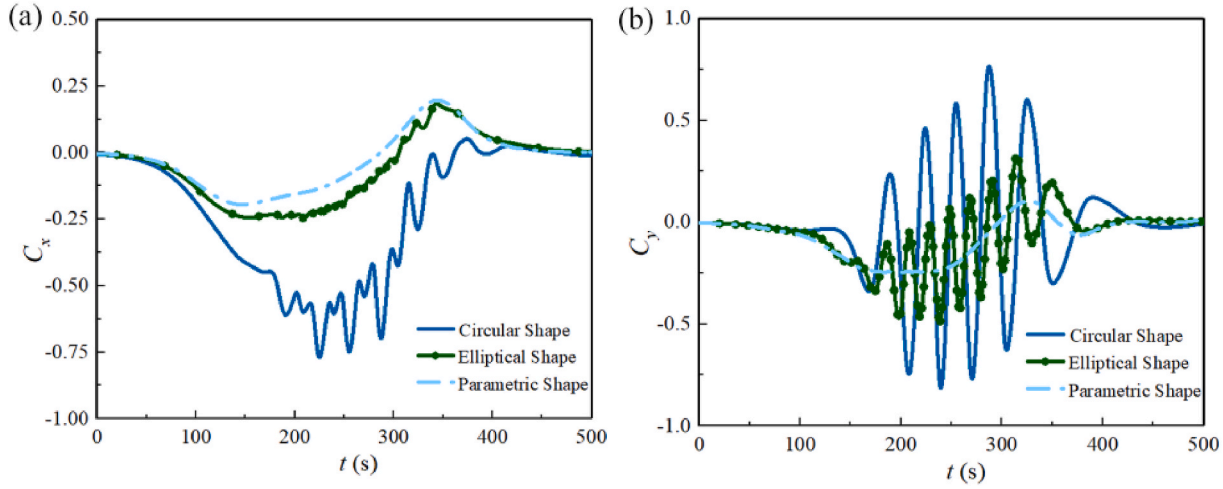

Fig. 7. Time series of force coefficients on the SFT for different SFT cross-sectional shapes. (a) Horizontal force coefficient (positive direction is ISW propagation direction); (b) vertical force coefficient (positive direction is upward).

$$A=\frac{2c_m}{3H'}\left\{\frac{H'-h_c}{h-h_c}\left[(H'-h_c)^3+(h-H')^3\right]+{h_c}^3\right\} \tag{6}$$

$$B=-\frac{c_m}{2(H'-h_c)^2} \tag{7}$$

$$h'=-\frac{\beta}{\alpha}\overline{h}-\frac{1}{\alpha}\left[(c_{mKdV}-c_m)B^{-1}+(\beta^2-\alpha)\overline{h}^2\right]^{0.5} \tag{8}$$

$$h''=-\frac{\beta}{\alpha}\overline{h}+\frac{1}{\alpha}\left[(c_{mKdV}-c_m)B^{-1}+(\beta^2-\alpha)\overline{h}^2\right]^{0.5} \tag{9}$$

$$\alpha=1+\frac{5}{4}\frac{H-H'}{H'} \tag{10}$$

$$\beta=1+\frac{1}{2}\frac{H-H'}{H'} \tag{11}$$

$$H=h_1+h_2,\overline{h}=h_2-h_c,H'=H-\frac{c_m^2}{g} \tag{12}$$

$$\frac{h_c^2(H-h_c)}{(H'-h_c)^3}=\frac{\rho_2}{\rho_1} \tag{13}$$

where h_1 and h_2 are the thickness of the upper-layer and lower-layer, respectively. ρ_1 and ρ_2 are the density of the upper-layer and lower-layer, respectively; H is total water depth; and h_c is the critical level. The polarity of the ISW is determined by the position of the interface with respect to the critical level h_c: when the interface is below (above) h_c the ISW is of elevation (depression).

The horizontal velocities of water particles in the upper and lower layers for a depression-type ISW are given by

$$u_i(x,t)=(-1)^{i+1}\frac{c_{mKdV}\zeta(x,t)}{h_i+(-1)^{i+1}\zeta(x,t)} \tag{14}$$

where $i=1,2$ represents the upper and lower layer fluids, respectively.

The characteristic "wavelength" of the mKdV ISW is expressed as

$$\lambda=2(H-h_c)\sqrt{\frac{(H-h_c)^3+{h_c}^3}{3Hh'h''}} \tag{15}$$

The integral frequency scale ω_m of the mKdV ISW is shown as

$$\omega_m=\frac{C_{mKdV}\kappa\mu^{1/2}}{\text{arctanh }\mu^{1/2}} \tag{16}$$

2.2. ISW properties

Based on field observations and high-resolution satellite images at Wenchang Station (112° E, 19°35′ N) (shown in Fig. 1) from April to October 2005, strong ISWs were identified in the continental shelf area, with the largest ISW amplitude 25–35 m, and the ISW packet near Hainan Island is dominated by the diurnal tide (Xu et al., 2010). As one of the potential SFT construction sites in China (Yan et al., 2016), (Zou et al., 2020a), the Qiongzhou Strait is close to Wenchang Station. Note that detailed reproduction of internal wave structure inside the strait is not the aim of this research, but rather to approximate the ISW's observed in the region for a conservative analysis of the SFT dynamic response. Therefore, the ISW characteristics recorded at Wenchang Station are applied for the analysis of hydrodynamic forces, serviceability, and reliability of the SFT in this study. Since the measured ISW amplitude is quite large compared with the strait depth of around 100 m, the mKdV theory is adopted for the ISW description in this study.

3. Numerical model

3.1. Model setup

Most SFT's have been designed with simple cross section shapes such as square, polygonal, circular, or elliptical. The circular and elliptical shapes exhibit more streamlined hydrodynamic behavior, experiencing smaller displacements and less stress than other bluff shapes (Gang et al., 2018), (Li and Jiang, 2016). A parametric method using Machine Learning to predict the optimal SFT cross-section shape for improving the hydrodynamic performance was presented in (Zou et al., 2020b), (Zou et al., 2020c), where the objective is to minimize the hydrodynamic forces (time-averaged drag and root mean square lift) on the SFT. The parametric shape has been compared with the simpler circular and elliptical shapes under extreme events (Zou et al., 2020a). In the current study, parametric, circular, and elliptical shapes for the SFT cross-section with equal clearance (5 m × 11 m), applied in previous research, are compared under ISW conditions. Assuming the tunnel wall thickness is 1 m, the maximum width and height of the parametric, circular, and elliptical shapes are 20 m × 10 m, 14 m × 14 m, and 16 m × 10 m, respectively.

A two-dimensional numerical ISW tank is generated using ANSYS Fluent to simulate the interaction between an ISW and the SFT (Fig. 2 (a)). The computational domain is 4500 m in length and 100 m in height, filled with a stratified two-layer fluid. The center of the SFT is located 200 m from the inlet. The thicknesses of the upper-layer and

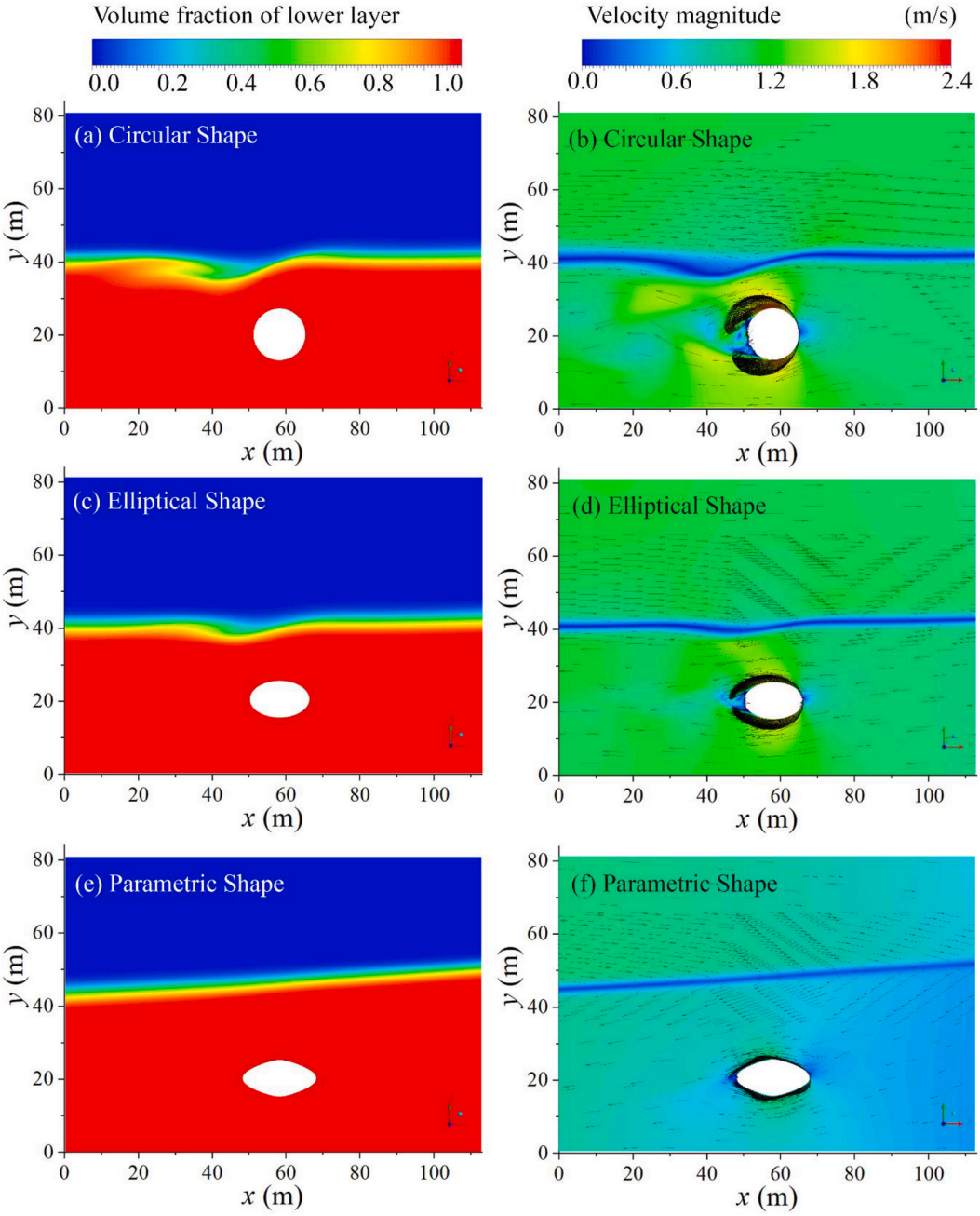

Fig. 8. The volume fraction and velocity field around the SFT for different SFT cross-sectional shapes. The SFT cross-sectional shapes from top to bottom are circle, ellipse, and parametric shape, respectively. The undisturbed ISW amplitude is 20 m.

lower-layer fluids are 30 m and 70 m, respectively. For a typical case the ISW, the amplitude a is selected as 20 m with a characteristic "wavelength" of 144 m. The densities of the fluids in the upper-layer and lower-layer are 1022 kg/m^3 and 1024 kg/m^3, respectively, based on the actual oceanic condition, in which the oceanic density difference is generally less than 3–4 kg/m^3 (Zhu et al., 2016). The VOF method (Hirt and Nichols, 1981) with a dispersed-type interface model is applied to capture the pycnocline.

Since the surface wave amplitude is relatively small compared with the ISW amplitude, the top boundary is assumed to be a "rigid lid" in all simulations. Freestream quantities of turbulence intensity and turbulence length scale are specified at the inlet boundary as per (Zou et al., 2020d). An outflow boundary is employed at the outlet. A simplified no-slip hydraulically smooth wall condition is applied on the SFT cross-section surface and the bottom boundary. The unsteady Reynolds-Averaged Navier-Stokes (URANS) equations with an RNG k -ε turbulence model are applied with a standard wall function. The reliability of this model for hydrodynamic force prediction of the SFT at high Reynolds numbers was verified by (Zou et al., 2020b).The URANS model was verified for its ability to provide sufficiently efficient and accurate ISW-induced force predictions (Liuet al., 2020) and vortex generation simulation (Hsu et al., 2004). However, the detection of small flow features such as vortex dynamics in the boundary layer should be simulated by LES or DNS models, which incur additional computation loads and are beyond the scope of this research. The computational domain is divided into several blocks of different resolutions (Fig. 2 (b)). The subdomain around the SFT cross-section surface is a 30 m × 30 m rectangular block with a high-quality unstructured mesh, including 40 layers of quadrangular cells that cover the boundary layer. The first grid layer cell thickness normal to the SFT surface is

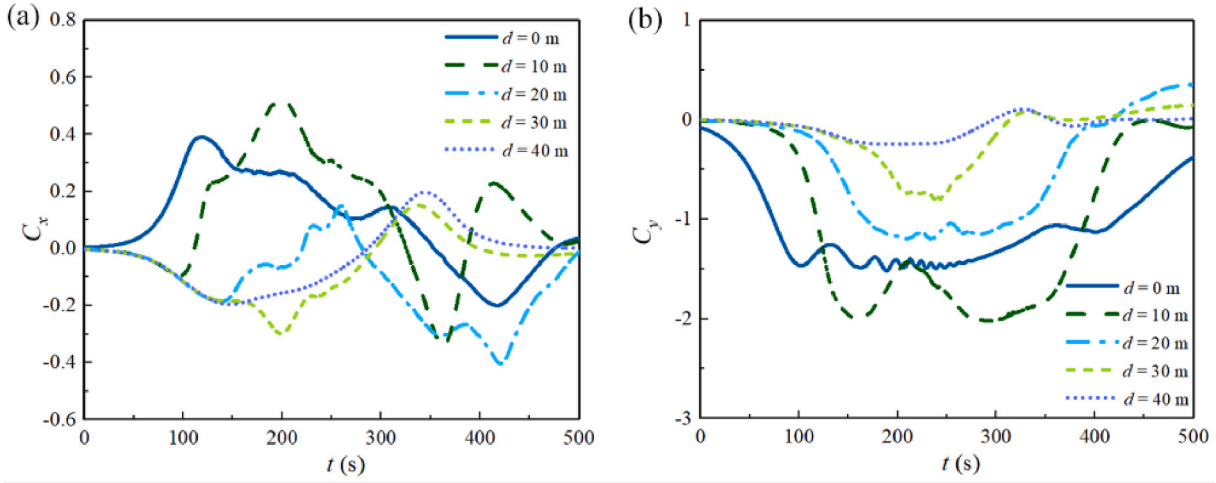

Fig. 9. Time series of force coefficients on the SFT for different SFT relative distances to the pycnocline. (a) Horizontal force coefficient (positive direction is ISW propagation direction); (b) vertical force coefficient (positive direction is upward).

0.003 m, within the acceptable range of y^+ at 30–200 (Kuzmin et al., 2007). Above this first cell, the cell thickness stretches with a growth rate of 1.2. The subdomain within the ISW propagation region has a horizontal and vertical mesh size of 2 m and 0.2 m, respectively. The adjacent subdomain crossing the SFT has a minimum grid size of 0.4 m. The structured mesh size in the rest of the subdomain is generally 2 m, and in the damping zone, an increasingly coarse mesh with a bias factor of 2 is set to cause extra numerical diffusion. An adaptive time-step was selected, and the maximum Courant number is set to 0.25. The PISO (Pressure-Implicit with Splitting of Operators) algorithm is used for pressure-velocity coupling. A high-performance computing (HPC) cluster is applied to run parallel computation tasks.

The direct inlet velocity prescription method is used to generate an ISW at the inlet boundary by a User Defined Function (UDF) (Ansys Inc, 2013), where the theoretical horizontal orbital velocities and surface elevation are imposed directly (Miquel et al., 2018), and the pressure is set to be hydrostatic. The UDF specifies the velocity components and fluid volume fraction for each cell on the boundary. Cavaliere et al. (2021) revealed that the pycnocline thickness affects ISWs kinematics. For a thick pycnocline layer condition, both the wave celerity and the velocity gradients decrease, and the hydrodynamic force on the SFT induced by the ISW is reduced. Therefore, as a conservative calculation of the hydrodynamic force on the SFT, only a thin pycnocline between the two-layer fluid is added. The thin pycnocline was set by a smooth "tanh" initial density distribution between the upper and lower layers as in (Ding et al., 2020), (Zhu et al., 2016). To avoid numerical instability at the interface, in this study, the ISW horizontal velocity distribution in the pycnocline layer is given by a linear velocity transition between the upper and lower layers, as shown in Eq. (17)

$$u(y) = -\frac{u_1 + u_2}{d_p}\left[y - \left(y_c - \frac{d_p}{2}\right)\right] + u_2 \tag{17}$$

where y is the vertical coordinate of the grid; y_c is the position of the mid-pycnocline layer; d_p is thickness of the pycnocline layer.

In order to determine the appropriate pycnocline layer thickness, a sensitivity analysis is carried out. We consider three different pycnocline layer thicknesses (0.05 m, 1 m, and 5 m). These are tested for the case with ISW amplitude of 20 m, SFT relative distance from the pycnocline of 10 m, and parametric cross section shape. In order to shorten the simulation time, fluid densities of 1022 kg/m^3 and 1054 kg/m^3 in the upper-layer and lower-layer are selected, respectively. Time series of the ISW-induced horizontal and vertical forces per meter on the SFT for each pycnocline layer thickness are shown in Fig. 3. It can be found that numerical instabilities occur (Fig. 3 (a)) with $d_p = 0.05$ m, while spikes can be effectively eliminated with $d_p = 1$ m or 5 m. However, as d_p increases to 5 m, the hydrodynamic forces on the SFT are underpredicted with a maximum force deviation around 2 kN compared to $d_p = 0.05$ m, whereas the difference in force computation between $d_p = 1$ m and 0.05 m is minor. This indicates that stable and accurate results are achieved with a pycnocline layer thickness of 1 m; and hence, $d_p = 1$ m is adopted in subsequent simulations.

For wave absorption, a dampening sink term given by Eq. (18) is added in the momentum equation within a damping length of 2000 m from the outlet boundary to avoid wave reflection (ANSYS, 2019).

$$S = -\left[C_1\rho v + \frac{1}{2}C_2\rho|v|v\right]f(x)f(y) \tag{18}$$

where C_1 and C_2 are linear and quadratic damping resistance, respectively; $f(x)$ and $f(y)$ are damping functions for inline and cross flow directions, respectively; v is flow vertical velocity. It features a combination of linear and quadratic damping, which allows the use of either one or a combination of both approaches. In this research, $C_1 = 10$ s^{-1}; $C_2 = 10$ m^{-1}.

3.2. Model validation

The dimensionless hydrodynamic force on an isolated cylinder is defined in Eq. (19).

$$C_{x,y} = \frac{F_{x,y}}{(\rho_2 - \rho_1)gA} \tag{19}$$

where F_x and F_y are horizontal and vertical force per meter on the cylinder, respectively; g is gravitational acceleration; and A is the cross-sectional area of the cylinder. Note that the forces on the cylinder are normalized in Eq. (19), and hence, $C_{x,y}$ is dimensionless. If ρ_1 is close to ρ_2, the hydrodynamic force $F_{x,y}$ will be close to 0. Thus, $C_{x,y}$ will not be infinite.

Numerical results are further verified by comparison to experimental data of horizontal force on the cylinder (Ermanyuk and Gavrilov, 2005) and an empirical formula. In this experiment, the fluid densities of the upper-layer and lower-layers are $\rho_1 = 1000$ kg/m^3 and $\rho_2 = 1021$ kg/m^3, respectively. The thicknesses of the upper-layer and lower-layers are $h_1 = 4$ cm and $h_2 = 8.5$ cm, respectively. The center of the1.5 cm diameter cylinder is located a distance of $h_0 = 9$ cm from the flume bottom. The ISW amplitude is 0.77 cm. Per the Morison Equation, the horizontal hydrodynamic load per meter can be estimated by the sum of the inertial and drag forces, given by Eq. (20)

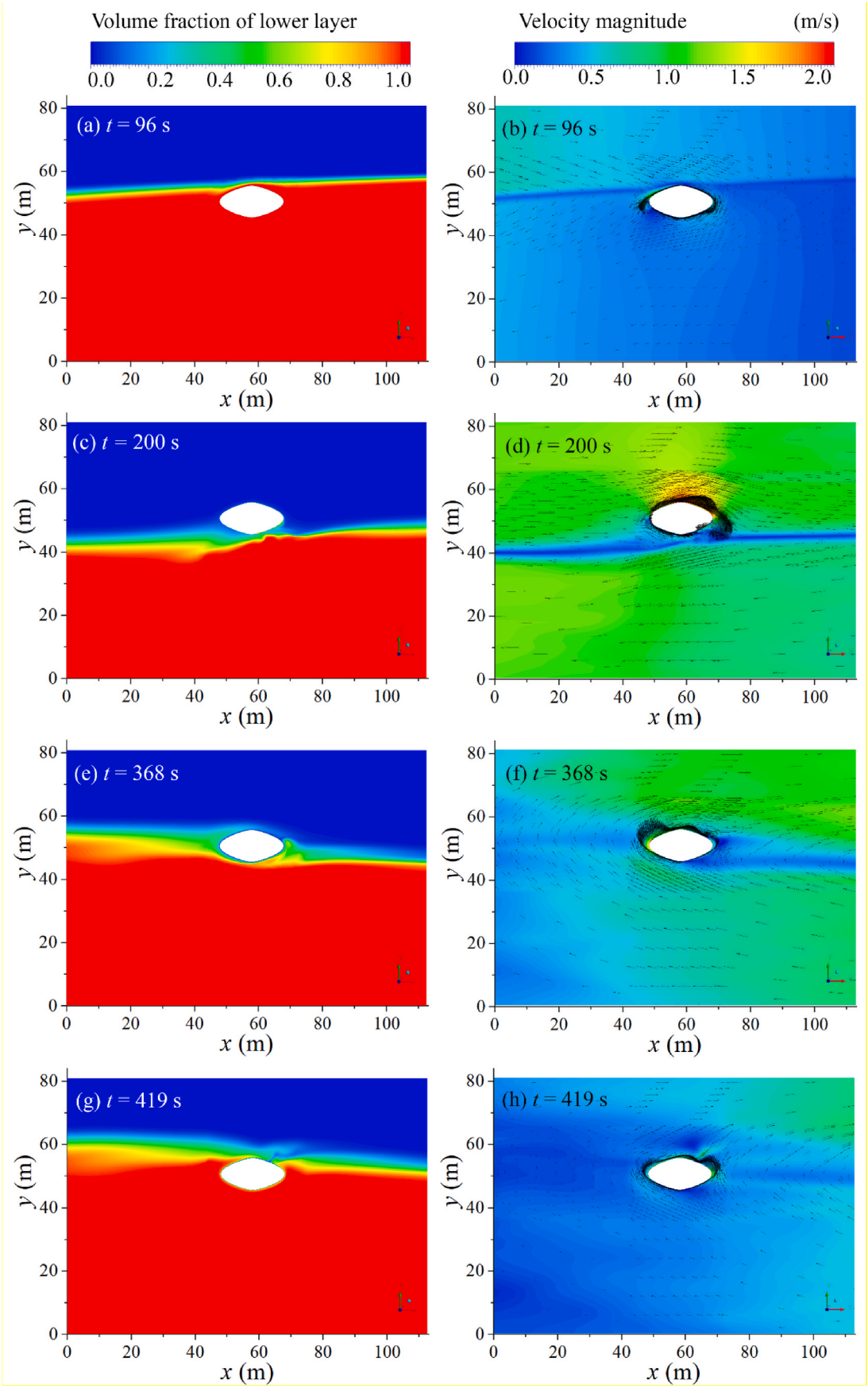

Fig. 10. The volume fraction and velocity field around the SFT for relative distance to the pycnocline of 10 m. The simulation times from top to bottom are 96 s, 200 s, 368 s, and 419 s, respectively. The undisturbed ISW amplitude is 20 m.

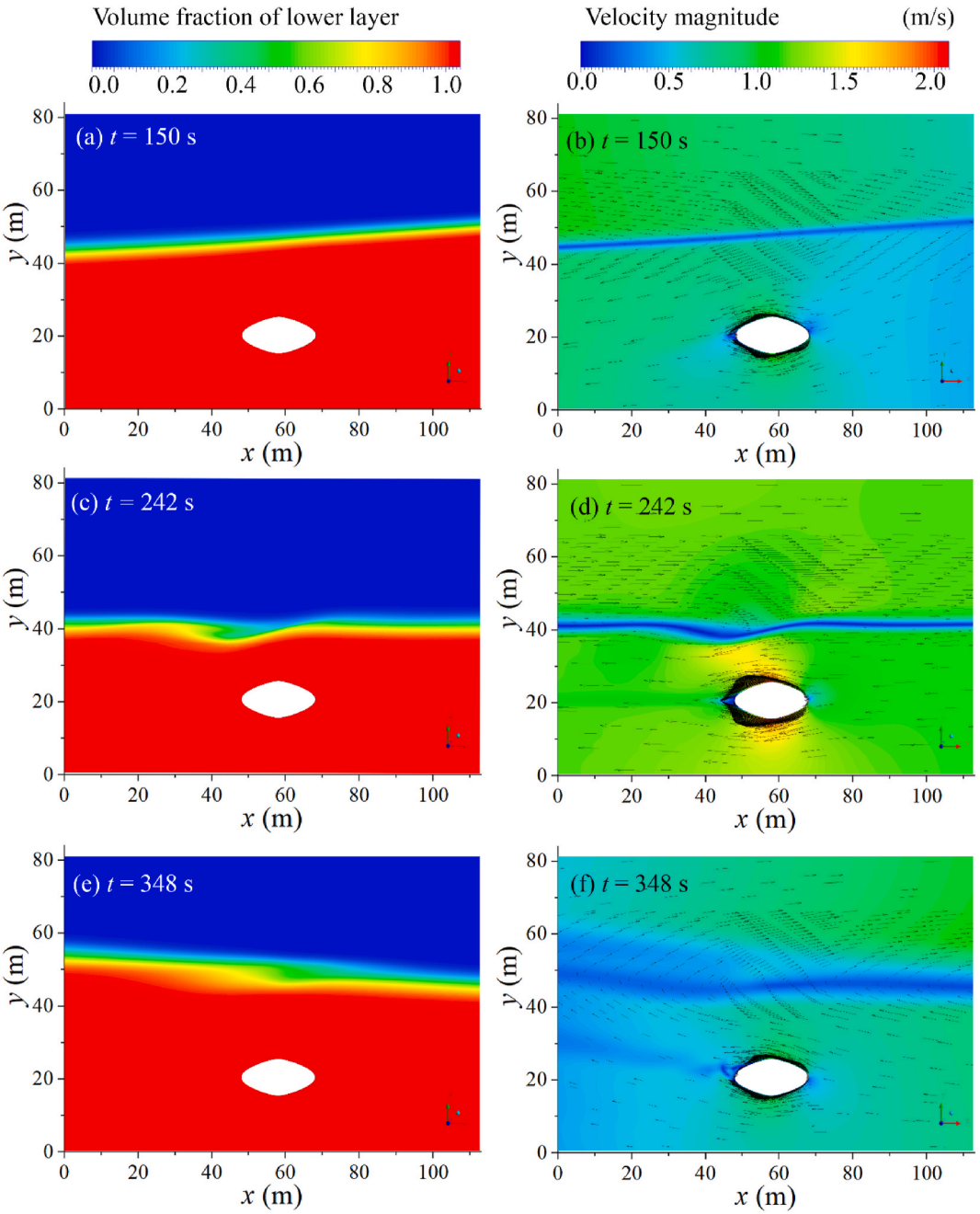

Fig. 11. The volume fraction and velocity field around the SFT for relative distance to the pycnocline of 40 m. The simulation times from top to bottom are 150 s, 242 s, and 348 s, respectively. The undisturbed ISW amplitude is 20 m.

$$F_x(t) = \frac{1}{2} C_d \rho D u|u| + C_m \rho A \frac{\partial u}{\partial t} \tag{20}$$

where u is the horizontal velocity component of the ISW fluid particles which can be computed by using Eq. (14); C_m and C_d are inertia and drag coefficients, respectively, and can be set as $C_m = 2.0$, $C_d = 1.2$, based on previous studies (Cai et al., 2006), (Cai et al., 2003).

The comparison of the horizontal hydrodynamic loads on the cylinder from each study is shown in Fig. 4, where Vt/H_0 is a dimensionless value from (Ermanyuk and Gavrilov, 2005). It illustrates that the Morison equation generally overpredicts the negative hydrodynamic force and underestimates the positive hydrodynamic force, while the numerical simulation results provide a better agreement with the experimental data. The discrepancy between the numerical and experimental results can be attributed to a difference of the ISW generation mechanism, where a hump-type ISW was produced by the wave-maker in the experiment, while the mKdV theory is applied in the numerical simulation.

To elucidate the mechanism of ISW-SFT interaction under oceanic conditions and investigate the influence of factors including the ISW amplitude, the SFT relative distance to the pycnocline (defined as the vertical distance between the centre position of the SFT and the initial location of the interface between the two-layers of fluids), the SFT cross-sectional shape, and fluid density on the SFT hydrodynamics, a sensitivity analysis is conducted by comparing the temporal variation of force coefficients on the SFT, the velocity and pressure fields in the vicinity of the SFT at specific moments, and the corresponding interface position of the two fluid layers.

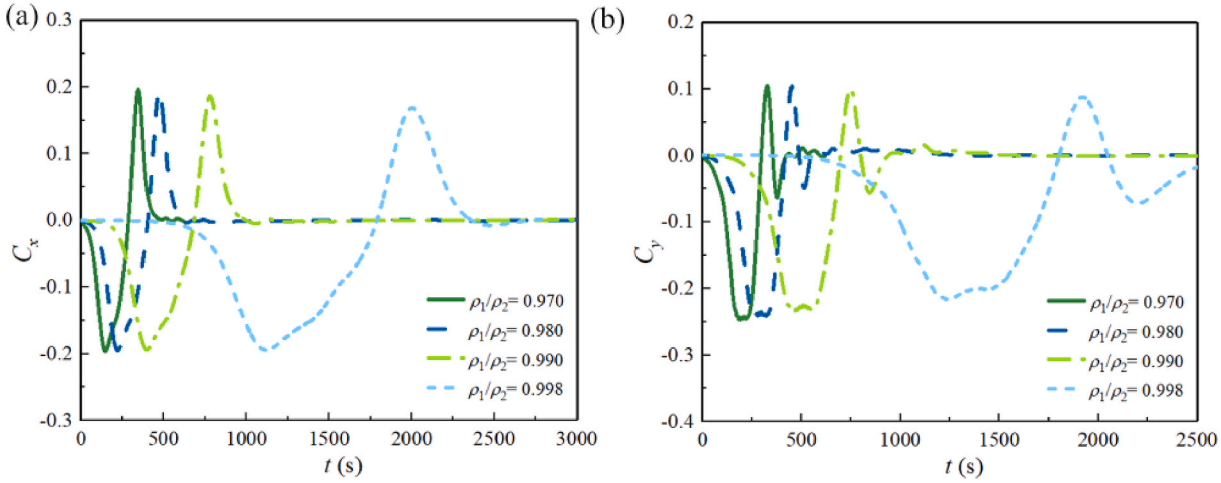

Fig. 12. Time series of force coefficients on the SFT for different fluid density ratios. (a) Horizontal force coefficient (positive direction is ISW propagation direction); (b) vertical force coefficient (positive direction is upward).

4. Sensitivity analysis of influence factors

4.1. Effect of ISW amplitude

Cases of ISW amplitude $a = 20$ m, 25 m, 30 m, and 35 m are selected, with a relative distance to the pycnoclilne of 40 m, parametric cross-sectional shape, and upper- and lower-layer densities of 1022 kg/m^3 and 1054 kg/m^3, respectively, to investigate the influence of ISW amplitude on the hydrodynamic force on the SFT.

Time series of force coefficient variation in horizontal and vertical directions for different ISW amplitudes are illustrated in Fig. 5. Positive horizontal force means the force direction is the same as the ISW propagation direction, and positive vertical force means the force direction is upward (assuming that the initial condition is when the SFT is neutrally buoyant). It can be found that C_x drops firstly to its negative maximum and undergoes a sharp increase to about double the maximum magnitude, followed by a plunge and oscillation around the equilibrium after the ISW passes over the SFT. It is worth noting that the larger the ISW amplitude is, the later the maximum negative force occurs. For a large ISW amplitude, the ISW can act on the SFT surface directly, and a strong interaction between the ISW and the SFT occurs, along with fluid mixing and wave dissipation and reflection, which prolongs the interaction time. Thus, the larger the ISW amplitude is, the later the maximum negative force occurs. However, according to Eqs. (1) and (14), the ISW's flow velocities increase with increasing the ISW's amplitude; and hence, the ISW with a large amplitude propagates faster than those smaller amplitude cases. The irregularity in the temporal distribution of C_x and C_y for large ISW amplitudes also indicates the complex mechanisms of the strong interaction between the ISW and the SFT. It can be deduced that reflected waves bounce back from the SFT, contributing to secondary peaks and interfacial instabilities. This also shows that the absolute maximum C_x and C_y increase with increasing ISW amplitude. The absolute maximum C_x reaches 0.6 at $a = 35$ m, while the absolute maximum C_y is 2.7.

Fig. 6 shows the volume fraction and velocity field distributions of the two layers of fluids when the horizontal force coefficient on the SFT reaches its negative maximum. Thus, different characteristics of the ISW-SFT interaction for various ISW amplitudes can be clearly elaborated. Note that the negative maximum of C_x increases with increasing ISW amplitude, which corresponds an increase of the ISW water particle velocity magnitude in each fluid layer. At $a = 20$ m (Fig. 6 (a, b)), the pycnocline keeps stable, and no evident deformation of the ISW profile or fluid mixing can be observed. However, at $a = 25$ m (Fig. 6 (c, d)), the ISW profile gets distorted, and mixing of fluids across the pycnocline is gradually generated above the leading-edge of the SFT. As the ISW trough approaches the SFT, the increasing velocities of both the convergence flow in the upper layer and divergence flow in the lower layer enlarge the shear stress at the interface, which enhances disturbance of the flow, and triggers mixing instabilities. The thickness of the mixing layer increases with increasing ISW amplitude. The flow area is partially blocked by the SFT, and the ISW profile distorts. The interface of the ISW is generally parallel to the upper left quadrant SFT surface and steepens with increasing ISW amplitude. The ISW energy is dissipated, and backflow and mixing are generated, making the flow field at the interface complex (Fig. 6 (d, f)). For $a = 35$ m (Fig. 6 (e, f)), as the ISW propagates, the ISW can act on the SFT surface directly, which can lead to reflection of the ISW. The irregularity at the local negative maximum of the horizontal force (Fig. 5 (a)) can be attributed to distortion of the ISW shape and strong interaction between the ISW and the SFT. However, C_x for $a = 35$ m does not show an increase after the ISW trough passes over the SFT compared with $a = 30$ m since the strong ISW-SFT interaction for $a = 35$ m dissipates the wave energy; therefore, the ISW amplitude is reduced after passing over the SFT.

4.2. Effect of SFT cross-section geometry

Circular, elliptical, and parametric SFT cross section shapes are investigated for an ISW amplitude of 20 m, relative distance to the pycnocline of 40 m, and upper- and lower-layer fluid densities of 1022 kg/m^3 and 1054 kg/m^3, respectively, to investigate the influence of the SFT cross-section shape on the hydrodynamic forcing of the SFT.

Time series of force coefficients in horizontal and vertical directions are illustrated in Fig. 7. The circular shape has the largest maximum absolute values of forces, while the parametric shape, with its streamlined curvature, generates the minimum forcing oscillation among the three shapes. It can also be found that C_x of all three shapes in both directions decreases at first, continuously increases afterward, and gradually decreases back to its equilibrium. The parametric shape experiences its negative maximum of C_x at 150 s, while the elliptical and circular shapes reach their negative maxima after 200 s. As shown in Fig. 7, the circular shape's force signal has a lower oscillation frequency than the elliptical shape.

Fig. 8 shows the volume fraction and velocity field distributions of the two layers of fluids when C_x on the SFT reaches its negative maximum. Characteristics of the ISW-SFT interaction as a function of SFT cross-sectional shape can be clearly elaborated. For the circular and elliptical cross-sectional shapes (Fig. 8 (b, d)), the negative maximum value of C_x generally occurs when the ISW trough is above the apex of

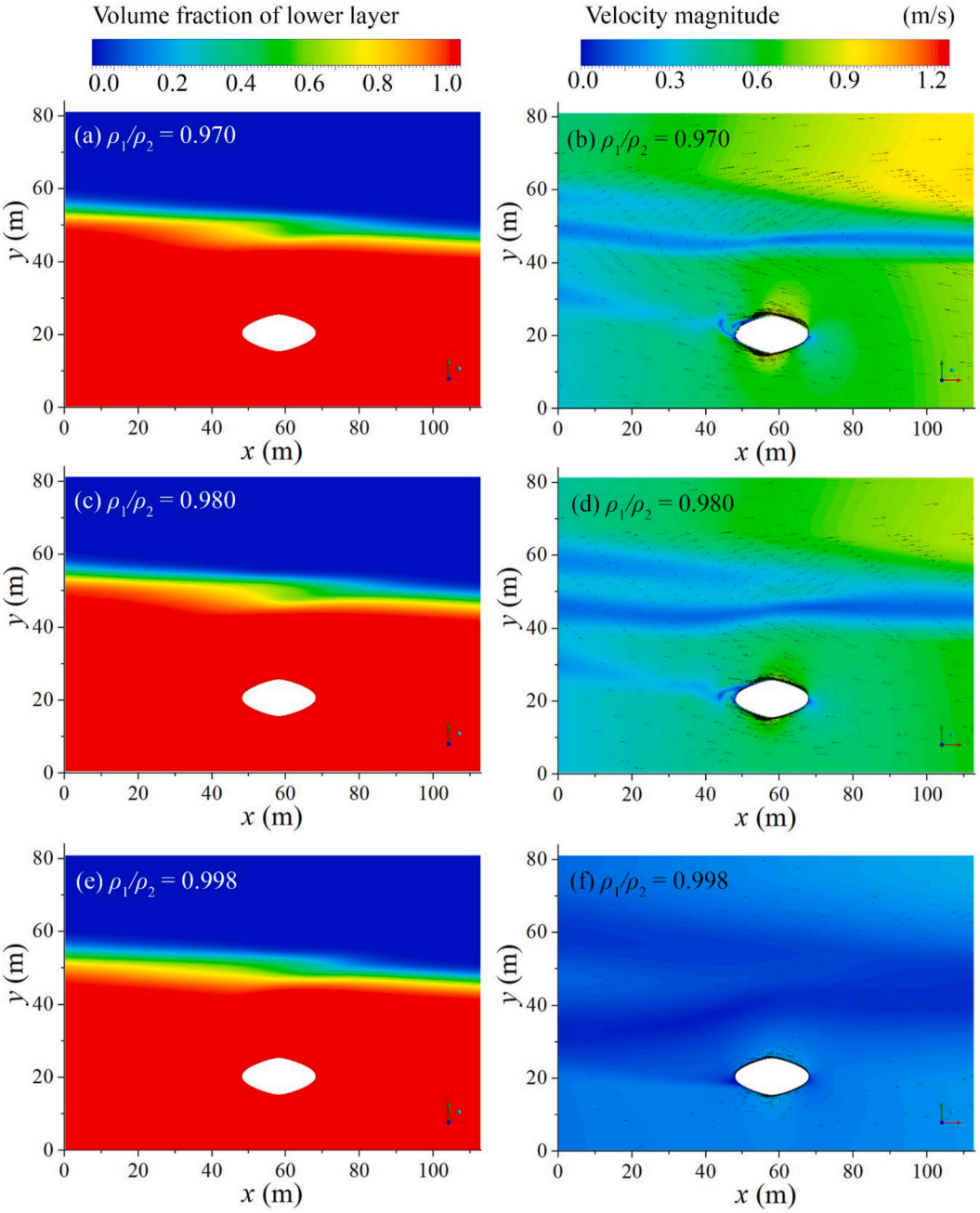

Fig. 13. The volume fraction and velocity field around the SFT for different fluid density ratios. The fluid density ratios, from top to bottom, are 0.970, 0.980, and 0.998 s, respectively. The undisturbed ISW amplitude is 20 m.

Table 1
Allowable deflection and motion limits for floating bridges (Lwin, 2000).

Loading Condition	Response direction	Maximum Deflection	Maximum Acceleration
Waves-dynamic	Vertical (heave)	±0.3 m	0.5 m/s^2
	Lateral (sway)	±0.3 m	0.5 m/s^2
	Rotation (roll)	±0.5°	0.05 rad/s^2

the SFT. The flow streamlines at the edges of the SFT are distorted by the bluff body, and the shape curvature in turn increases the velocity magnitude at the apex and nadir points. Furthermore, as the flow passes over the SFT, the shear stress near the SFT surface grows, and the flow separates from the SFT due to the strong adverse pressure gradient (APG) resulting from the shape curvature, triggering a wide wake recirculation regime and periodic vortex shedding at the left edge (note that the ISW trough travels to the right, resulting in flow toward the left in the lower fluid layer). The vortex shedding process, together with the steady pressure gradient, amplifies the gross hydrodynamic force on the SFT. The horizontal force induced by vortex shedding partially compensates for the reduction in horizontal force when the ISW trough is above the SFT (Fig. 7 (a)). From Fig. 7 (b), the frequency of vortex shedding can be estimated to be around 0.03 Hz. The intrinsic ISW characteristic frequency is 0.0078 Hz based on Eq. (16). It can be deduced that the vortex shedding frequency is much faster than the intrinsic ISW characteristic frequency. Vortex shedding affects the SFT around 170 s before the ISW trough passes over the SFT, and dissipates after the back shoulder of the ISW passes over the right edge of the SFT at around 380 s. If the vortex shedding frequency is close to the structural natural frequency, the occurrence of fatigue damage to the SFT

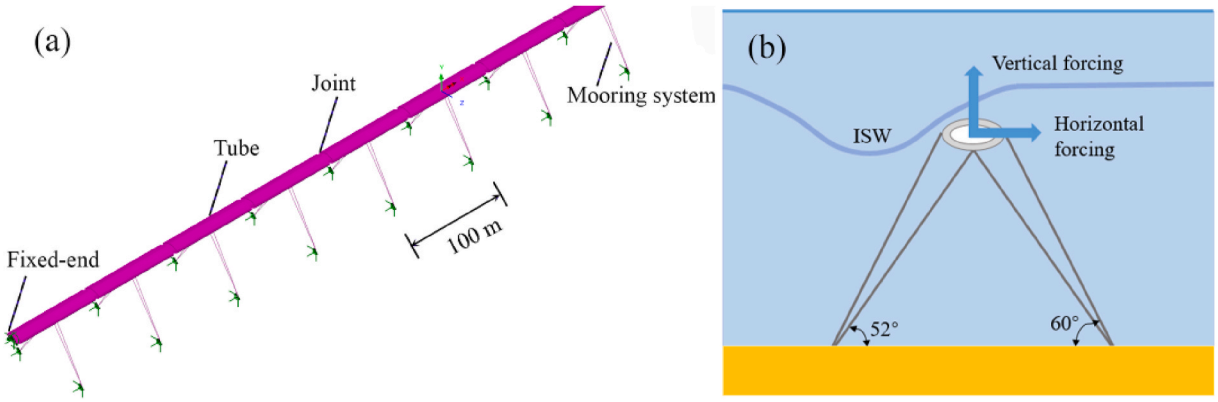

Fig. 14. One portion of the SFT FEM model; (a) Coupled tube-joint-mooring system; (b) Mooring lines arrangement (front view).

Table 2
Structure and Material parameters.

Item	Parameter	Value
Tunnel tube	Young's modulus (GPa)	40.2
	Gross density with added mass (kg/m^3)	6088
	Tunnel wall thickness (m)	1.0
	Cross-sectional area (m^2)	43.8
Mooring line	Mooring interval (m)	100
	Nominal diameter (m)	0.18
	Mass/Unit length (kg/m)	644.7
	Added mass coefficient	1.0
	Minimum breaking load (kN)	30689 (Grade R5)
Tunnel joint	Axial stiffness (GN/m)	22.1
	Shear stiffness (GN/m)	0.76
	Bending stiffness (GN·m/rad)	548
	Torsional stiffness (GN·m/rad)	592

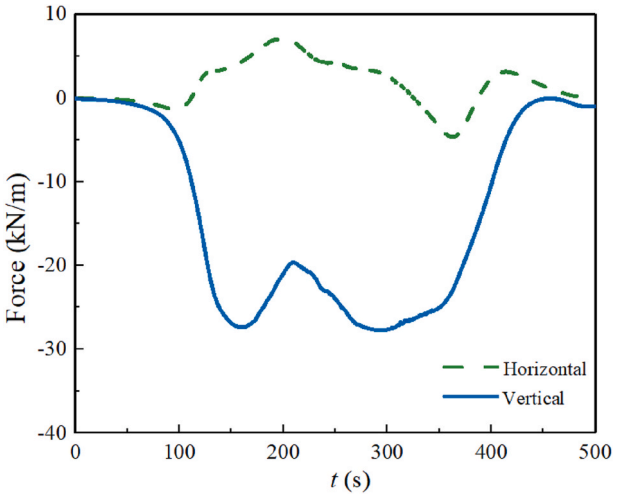

Fig. 15. The selected ISW-induced force on the SFT with $a = 20$ m, $d = 10$ m, parametric cross-sectional shape, and $\rho_1/\rho_2 = 0.970$.

tube and its support connections should be considered as a design criterion. The circular shape with its large curvature increases the form drag on the SFT. The ISW profile shoals above the circular shape, and the distorted wave profile entrains the fluid from the upper layer into the lower layer, causing significant fluid mixing, strong ISW-SFT interaction, and energy dissipation (Fig. 8 (a, b)). Furthermore, for the circular shape, Fig. 7 shows that the hydrodynamic force induced by vortex shedding dominates the oscillation of vertical force on the SFT, whereas the parametric shape experiences reduced flow separation and vortex shedding.

4.3. *Effect of SFT relative distance to pycnocline*

The dimensionless relative distance of the SFT to the pycnocline is defined as the vertical distance between the centre position of the SFT and the initial interface between the two fluid layers. Cases with SFT relative distance of $d = 0$ m, 10 m, 20 m, 30 m, and 40 m are selected with an ISW amplitude of 20 m, parametric cross-sectional shape, and upper- and lower-layer densities of 1022 kg/m^3 and 1054 kg/m^3, respectively, to investigate the influence of the SFT relative distance to the pycnocline on the hydrodynamic forcing of the SFT. Forces on the SFT for different relative distances from the SFT to the pycnocline are shown in Fig. 9. The oscillatory component of force on the SFT is quite different with different relative distances, due to a complex combination of buoyancy, drag, and inertia force contributions. Apart from the case of $d = 0$ m, the absolute maximum force on the SFT decreases with increasing relative distance. The maximum horizontal force coefficient is for $d = 10$ m, with a value of $C_x = 0.5$, while the absolute maximum C_y is for $d = 10$ m with a value of $|C_y| = 2.0$.

In order to further elaborate the effect of relative distance on the forces affecting the SFT, the evolution of the pycnocline location and velocity field in the vicinity of the SFT at different time instants are explored for the cases relative distance of 10 m and 40 m. For $d = 10$ m (Fig. 10), as the ISW propagates and approaches the SFT, the SFT is fully submerged in the bottom-layer fluid at the outset. The horizontal water particle velocity above the upper left quadrant surface of the SFT increases when the SFT's front shoulder touches the top left edge of the SFT at 96 s due to the narrowed flow cross-sectional area (Fig. 10 (a, b)). The increased pressure acting on the right edge increases the horizontal force on the SFT until its local negative maximum is reached (Fig. 9 (a)). Afterward, the ISW profile is distorted when it interacts with the SFT and separates into two parts: one part of the ISW is transmitted over the SFT and the other part is reflected. Assuming that the initial condition is when the SFT is neutrally buoyant; as the front shoulder of the ISW gradually crosses over the SFT, the buoyancy continuously reduces while the vertical force increases (Fig. 9 (b)) until the interface between the two layers of fluid hits the lower surface of the SFT at 200 s (Fig. 10 (c, d)). The upper surface of the SFT is fully submerged in the upper layer fluid and the tangential water particle velocity increases near SFT apex at 200 s, while the velocity near the lower surface reduces to 0. This ultimately causes a clear velocity difference between the upper and lower half of the SFT, inducing an upward force on the SFT, shown as a "hump" in Fig. 9 (b). The water particle velocity near the right edge half is generally higher than near the left edge half. Furthermore, a small amount of reverse flow is generated below the lower right edge, enhancing the force on the SFT (Fig. 9 (a)). At around 368 s, the back shoulder of the ISW hits the SFT (Fig. 10 (e, f)), increasing the local

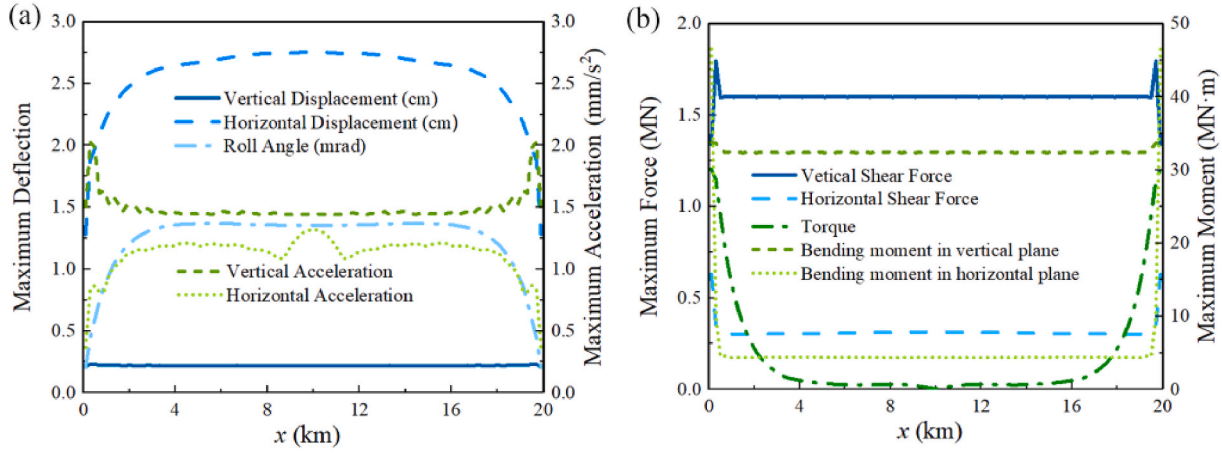

Fig. 16. (a) Envelopes of the maximum tube motion; (b) Envelopes of the maximum tube internal forcing.

water particle velocity. The increased pressure acting on the right edge increases the horizontal force to its local negative maximum (Fig. 9 (a)). Similarly, as the back shoulder of the ISW crosses over the SFT, the buoyancy of the SFT continuously increases (Fig. 9 (b)), and as the back shoulder of the ISW hits the SFT upper right quadrant at 419 s (Fig. 10 (g, h)), the water particle velocity magnitude near the right edge surface increases, and hence, the horizontal force ranks to its local positive peak value (Fig. 9 (a)). Also note that the fluid mixing layer thickness increases as the ISW propagates and interacts with the SFT.

For $d = 40$ m (Fig. 11), the forcing time series on the SFT is less complex because the SFT is fully submerged in the bottom layer during the whole ISW propagation process. When the ISW front shoulder passes above the SFT, the horizontal water particle velocity is opposite the ISW propagation direction, generating a stagnation point at the upper right quadrant. The flow velocity rapidly increases near the lower surface of the SFT, resulting in a larger dynamic pressure (so lower static pressure in the non-stagnated area) along the lower surface than the upper half of the SFT (Fig. 11 (a, b)).Both the horizontal and vertical forces in Fig. 9 decrease at $t = 150$ s. When the ISW trough propagates above the SFT apex at around 242 s (Fig. 11 (c, d)), the stagnation point at the rear moves to the right edge tip, and the dynamic pressure difference between the right and left quadrants of the SFT decreases. As the ISW back shoulder propagates above the SFT at 348 s (Fig. 11 (e, f)), the stagnation points at the rear moves to the lower surface. At the same time, water particle speed acting on the upper right surface is higher than the lower right surface. The flow separates and forms a wake region at the left edge, which increases the pressure difference between the front and rear surfaces of the SFT, resulting in an increase in the horizontal force (Fig. 9 (a)). From Fig. 9 (b), it is clear that the vertical force on the SFT is affected significantly by the relative distance of the SFT to the pycnocline. The buoyancy of the SFT also changes significantly as a function of the relative distance to the pycnocline, and contributes to the vertical force, leading to a clear enhancement of the vertical force on the SFT for $d = 10$ m compared with $d = 40$ m. It can be deduced that in this study, the buoyancy change dominates the vertical force distribution.

However, we note that the results above partially contradict the achievements by Ermanyuk (Ermanyuk and Gavrilov, 2005) and Ding et al. (2020), which concluded that the horizontal load is maximum when the cylinder is located on the bottom of the flume and is minimum when the cylinder is near the interface. This discrepancy is induced by the ISW properties, and the ratio of ISW amplitude to SFT cylinder cross-section diameter is very different. With the confined model scales and a small ISW amplitudes of their studies, they did not observe the complex flow field, strong interaction between ISW and structure, nor the dramatic buoyancy shift of the structure seen in our research. This underscores the necessity of large-scale modeling of the SFT under real oceanic conditions that cannot be simulated in laboratory experiments. Note that the existence of buoyancy change and large velocity gradients at the fluid interface induces prominent vertical loads and shear flows, which should be further evaluated in dynamic structural analysis.

4.4. *Effect of fluid density*

Cases with the fluid density ratio of the two layers $\rho_1/\rho_2 = 0.970$, 0.980, 0.990, and 0.998 with a fixed upper-layer density of 1022 kg/m^3 but varying lower-layer density are selected. An ISW amplitude of 20 m, relative distance to the pycnocline of 40 m, and parametric cross-sectional shape are used for all the cases, to investigate the influence of the fluid density on the hydrodynamic forcing of the SFT.

Fig. 12 illustrates that the absolute maximum of the force coefficient remains almost unchanged for different fluid density ratios, indicating the fluid density ratio is not a crucial factor for the dimensionless hydrodynamic force on the SFT. According to Eq. (19), the ISW-induced hydrodynamic force on the SFT is generally proportional to the fluid density difference. Per the mKdV theory in Eq. (14), the convection-diffusion process is inhibited as the fluid density ratio increases, due to the decrease of travelling wave speed. Fig. 13 shows the volume fraction and velocity field distributions in the two layers when C_x reaches its positive maximum. As the fluid density ratio increases, the velocity magnitude of water particles decreases in both the upper- and lower-layers. Also, the water particle speed at the nadir/apex of the SFT decreases with increasing fluid density ratio. However, from Fig. 13 (b, d, f), it is seen that the thickness of fluid mixing at the interface increases with increasing fluid density ratio.

5. Dynamic responses analysis

5.1. *Structural serviceability requirements*

The SFT, as a flexible structure, allows deflections and accelerations to a certain extent. However, deflection and acceleration affect the serviceability of the structure and human perception of comfort, making it a vital metric for reliability assessment of the structure. Structural deflection and acceleration are related to the serviceability limit state (SLS) for the SFT to perform its intended function. Furthermore, structural vibration duration, frequency, and direction affect human tolerance to the SFT's motion. Due to the absence of design criteria for serviceability requirement of an SFT, the design code of similar structures such as movable highway bridges, floating bridges, and fixed bridges can be applied per (Aashto, 2010), (Koglin, 2003). Motion criteria focused on assurance of human comfort while walking or driving on floating bridges is assessed using normal storm (1-year storm)

conditions, and the serviceability limits for deflection and acceleration are listed in Table 1.

5.2. Structural dynamic response analysis

In order to examine the ISW impact on the dynamic response of the SFT to oceanic conditions, the finite element method (FEM) software LUSAS v15.2 (F. E. A. LTD) is employed for prototype SFT modelling. A case study of an SFT built in the Qiongzhou Strait is adopted to demonstrate the feasibility and applicability based on structural dynamic behavior prediction. Since the Qiongzhou Strait is regarded as one of the potential SFT application sites in China, requiring for a tunnel length of about 20 km, a three-dimensional SFT model of coupled tube-joint-mooring components with a total length of 20 km and tunnel element length of 100 m is generated in this study. Tunnel tube section elements and mooring lines are modeled as "Thick Beams (BMS3)", and tunnel joints are simulated as "Point Joints (JSH4)" with six degrees of freedom (DOF), including three linear spring units and three torque spring units. The total number of elements is 4599. The shear and bending stiffness of the tunnel joint in vertical and horizontal directions are assumed as the same. Mooring lines with a longitudinal spacing of 100 m are arranged symmetrically to balance restoring forces. An internal rigid constraint is applied to each mooring end at the tube, and the other mooring end connecting the seafloor is a rotational release. Both ends of the tunnel tube are fixed. The added mass of the tube is assumed to be a constant value and the gross density (including added mass) of the tube is taken as 6088 kg/m^3. The classical mass and stiffness dependent Rayleigh damping is selected and shown in Eqs. (21) and (22).

$$\beta_1 = \xi \frac{2\omega_i \omega_j}{\omega_i + \omega_j} \tag{21}$$

$$\beta_2 = \xi \frac{2}{\omega_i + \omega_j} \tag{22}$$

where β_1 and β_2 are the real-valued mass and stiffness proportional damping coefficients; ξ is modal damping ratio; ω_i and ω_j are the i th and j th mode natural frequencies of the SFT system, respectively.

The structural damping limits the SFT hydro-elastic response, with the Rayleigh damping coefficients β_1 and β_2 determined by the dominant structural natural frequencies and taken as 0.02 and 0.03, respectively. The FEM model and material settings are described in Fig. 14 and Table 2, and detailed model descriptions can be referred to in our previous research (Zou et al., 2021). For fluid and structure coupling, two-way fully coupled three-dimensional fluid-structure interaction (FSI) simulation is particularly time-consuming. An alternative approach is presented in this study which simplifies the hydrodynamic load into two-dimensions. The fluid pressure acting on the SFT is transferred to the FEM model, while the effects of displacement and deformation of the SFT on the flow field are neglected in the one-way FSI model. The applied shear stiffness of the tunnel joint (Table 2) is less than the axial stiffness, which means the hydrodynamic load direction transverse to the tunnel tube in the horizontal plane is more critical than the longitudinal direction. Therefore, the scenario of ISW-induced force transverse to the tube is considered more conservative than oblique internal wave loading conditions. Furthermore, as per (Chen et al., 2020), the effect of ISW direction on the vertical force on the SFT is negligible. Therefore, as a conservative scenario, the applied external ISW-induced dynamic load is assumed to be uniformly distributed along the tube element nodes, in a direction transverse to the tunnel span. This uniformly distributed load along the fixed-end tube is regarded as one of the worst case scenarios, because it generates the largest shear force at the end of tube, in addition to large bending moments at both mid-span and tube ends. A tube submergence depth of 40 m, corresponding to the case d = 10 m in section 3.5, is selected for structural dynamic simulation, in which the influence of buoyancy shift on the SFT can be clearly seen, as shown in Fig. 15.

Fig. 16 (a) depicts the envelopes of the tube deflection and acceleration in both horizontal and vertical directions under the ISW. It is observed that the maximum deflection of the tube is about 2.75 cm at mid-span, while the maximum acceleration of the tube is about 2 mm/s^2 near the shore connections. However, these values are far less than that of the aforementioned structural severability requirements (Table 1), implying the effect of internal waves on the dynamic motions of the SFT tube is negligible. This is because, unlike the surface waves for which the wave frequency may overlap the structural natural frequency and amplify the structural response (Zou et al., 2021), the frequency of the ISW is much lower than the natural frequency of the SFT tube. Therefore, the SFT is not prone to the resonance with the ISW.

Fig. 16 (b) shows the envelope of the internal force in the SFT tube along the span under the ISW. The maximum shear force reaches 1.8 MN in the vertical direction, and the maximum bending moment in the horizontal plane can be over 45 MN m near the shore connection due to the end constrains. Even though the displacement and acceleration of the SFT subjected to the ISW are relatively small, the large shear force and bending moment due to the buoyancy shift induced by ISW still affects BWR, and ultimately the tension force in the mooring lines. This can threaten the safety and reliability of the SFT system, which should be carefully examined during engineering design.

6. Conclusion

In this paper, the CFD software Fluent is applied to simulate the oceanic ISW's generation and propagation. The mechanism of interaction between the ISW and SFT is revealed by elucidating the velocity fields around the SFT during the ISW propagation. The fluid mixing process between the two layers and the shape of the ISW profile are compared among different conditions. The forces induced by ISW on the SFT are calculated under various cases of ISW amplitude, SFT cross-sectional shape, relative distance of the SFT to the pycnocline, and fluid density ratio. The structural motion response and dynamic forcing of a super-long SFT composed of a coupled tube-joint-mooring system are assessed under oceanic ISW conditions. The main conclusions are briefly summarized as follows:

(1) The maximum SFT forces in both horizontal and vertical directions and the thickness of the mixing layer increase with increasing ISW amplitude. Strong ISW-SFT interaction and severe energy dissipation can be found when the ISW amplitude is large.
(2) The most streamlined SFT cross section geometry (the parametric shape) experiences reduced flow separation and vortex shedding, as well as the minimum ISW-induced force, compared with the circular and elliptical shapes. Furthermore, the ISW-induced forces on the parametric cross section shape SFT are mainly caused by the pressure gradient, while vortex shedding contributes comparatively larger forces on the SFT with the circular shape.
(3) The influence of the relative distance from the SFT to the pycnocline is crucial due to a complex combination of buoyancy, drag, and inertia force contributions. The buoyancy change induced by the ISW evolution can remarkably alter the vertical force and BWR of the SFT. It is imperative to simulate a prototype SFT under real ISW conditions including a complex flow field, strong interaction between the ISW and structure, and the structural buoyancy change.
(4) The ISW-induced forces on the SFT are proportional to the fluid density difference. The fluid mixing thickness at the interface increases with increasing fluid density ratio.
(5) The deflections and accelerations of the SFT under the ISW are far smaller than the structural serviceability requirements of floating bridges. As the ISW is a long wave, its frequency is much lower

than the natural frequency of the SFT tube. Therefore, resonance of the tunnel tube under ISW conditions becomes unlikely.

(6) Due to BWR change during the ISW evolution, a large shear force and bending moment on the SFT may occur, which affects the tension force in the mooring lines, and can threaten the safety and reliability of the SFT system.

Nevertheless, it should be clarified that in the present study, the ISW-induced forces on the SFT are assumed to act uniformly and transverse to the tunnel tube as a worst-case scenario. Discrepancy in the dynamic response estimation can be induced by the two-dimensionality of hydrodynamic forces and by neglect of the impacts on the surrounding fluid field of structure deformation and movement. A related and practical hazard comes from ISW fissions into rank-ordered packets of internal solitons, which can propagate shoreward from the edge of the continental shelf; the impacts of internal wave packets on the SFT should be also be investigated in follow-on research.

CRediT authorship contribution statement

P.X. Zou: Investigation, Data curation, Formal analysis, Methodology, Validation, Visualization, Writing – original draft. **Jeremy D. Bricker:** Conceptualization, Methodology, Supervision, Writing – review & editing. **Wim.S.J. Uijttewaal:** Supervision, Writing – review & editing.

Declaration of competing interest

The authors declare that they have no known competing financial interests or personal relationships that could have appeared to influence the work reported in this paper.

Acknowledgement

The study presented in this paper was conducted in the submerged floating tunnel research project funded by China Communications Construction Company Ltd. (CCCC).

References

Aashto, 2010. AASHTO LRFD Bridge Design Specifications.
ANSYS, F., 2019. ANSYS Fluent Theory Guide 19.1. ANSYS, Canonsburg, PA.
Ansys Inc, 2013. ANSYS Fluent UDF Manual. Knowl. Creat. Diffus. Util.
Cai, S., Long, X., Gan, Z., 2003. A method to estimate the forces exerted by internal solitons on cylindrical piles. Ocean Eng. https://doi.org/10.1016/S0029-8018(02)00038-0.
Cai, S., Wang, S., Long, X., 2006. A simple estimation of the force exerted by internal solitons on cylindrical piles. Ocean Eng. https://doi.org/10.1016/j.oceaneng.2005.05.012.
Cai, S., Long, X., Wang, S., 2008. Forces and torques exerted by internal solitons in shear flows on cylindrical piles. Appl. Ocean Res. https://doi.org/10.1016/j.apor.2008.03.001.
Cavaliere, D., la Forgia, G., Adduce, C., Alpers, W., Martorelli, E., Falcini, F., 2021. Breaking location of internal solitary waves over a sloping seabed. J. Geophys. Res. Ocean. 126 (2) https://doi.org/10.1029/2020JC016669.
Chen, M., Chen, K., You, Y.X., 2017. Experimental investigation of internal solitary wave forces on a semi-submersible. Ocean Eng. https://doi.org/10.1016/j.oceaneng.2017.06.027.
Chen, M., Chen, J., You, Y.X., 2020. Forces on a semi-submersible in internal solitary waves with different propagation directions. Ocean Eng. https://doi.org/10.1016/j.oceaneng.2020.107864.
Cui, J., Dong, S., Wang, Z., Han, X., Yu, M., 2019. Experimental research on internal solitary waves interacting with moored floating structures. Mar. Struct. https://doi.org/10.1016/j.marstruc.2019.102641.
Ding, W., Ai, C., Jin, S., Lin, J., 2020. Numerical investigation of an internal solitary wave interaction with horizontal cylinders. Ocean Eng. https://doi.org/10.1016/j.oceaneng.2020.107430.
Ermanyuk, E.V., Gavrilov, N.V., 2005. Experimental study of the dynamic effect of an internal solitary wave on a submerged circular cylinder. J. Appl. Mech. Tech. Phys. https://doi.org/10.1007/s10808-005-0137-y.
F. E. A. LTD, "LUSAS User Manual." (Version).
Gang, L., Xiao-jun, Z., Jian-xun, C., 2018. The dynamic response of an experimental floating tunnel with different cross sections under explosive impact. J. Coast Res. https://doi.org/10.2112/si82-031.1.
Hibiya, T., 1986. Generation mechanism of internal waves by tidal flow over a sill. J. Geophys. Res. https://doi.org/10.1029/jc091ic06p07697.
Hirt, C.W., Nichols, B.D., 1981. Volume of fluid (VOF) method for the dynamics of free boundaries. J. Comput. Phys. https://doi.org/10.1016/0021-9991(81)90145-5.
Hsu, T.W., Hsieh, C.M., Hwang, R.R., 2004. Using RANS to simulate vortex generation and dissipation around impermeable submerged double breakwaters. Coast. Eng. 51 (7) https://doi.org/10.1016/j.coastaleng.2004.06.003.
Kakutani, T., Yamasaki, N., 1978. Solitary waves on a two-layer fluid. J. Phys. Soc. Japan. https://doi.org/10.1143/JPSJ.45.674.
Klymak, J.M., Pinkel, R., Liu, C.T., Liu, A.K., David, L., 2006. Prototypical solitons in the South China sea. Geophys. Res. Lett. https://doi.org/10.1029/2006GL025932.
Koglin, T.L., 2003. Movable Bridge Engineering.
Koop, C.G., Butler, G., 1981. An investigation of internal solitary waves in a two-fluid system. J. Fluid Mech. https://doi.org/10.1017/S0022112081000372.
Kuzmin, D., Mierka, O., Turek, S., 2007. On the implementation of the fr-fturbulence model in incompressible flow solvers based on a finite element discretisation. Int. J. Comput. Sci. Math. https://doi.org/10.1504/ijcsm.2007.016531.
Li, K., Jiang, X., 2016. Research on Section Form of Submerged Floating Tunnels Considering Structural Internal Force Optimization under Fluid Action. https://doi.org/10.1016/j.proeng.2016.11.551.
Lin, Z., Zan, X., 2021. Numerical study on load characteristics by internal solitary wave on cylinder sections at different depth and its parameterization. Ocean Eng. https://doi.org/10.1016/j.oceaneng.2020.108343.
ling Wang, L., Xu, J., Wang, Y., Wei, G., Lin, C., Zhu, H., 2018. Reduction of internal-solitary-wave-induced forces on a circular cylinder with a splitter plate. J. Fluid Struct. https://doi.org/10.1016/j.jfluidstructs.2018.08.015.
Liu, S., et al., 2020. Resistance and flow field of a submarine in a density stratified fluid. Ocean Eng. 217 https://doi.org/10.1016/j.oceaneng.2020.107934.
Lü, H., Xie, J., Xu, J., Chen, Z., Liu, T., Cai, S., 2016. Force and torque exerted by internal solitary waves in background parabolic current on cylindrical tendon leg by numerical simulation. Ocean Eng. https://doi.org/10.1016/j.oceaneng.2016.01.028.
Lwin, M.M., 2000. Floating bridges. Bridg. Eng. Handb. 22, 1–23.
Michallet, H., Barthélémy, E., 1998. Experimental study of interfacial solitary waves. J. Fluid Mech. https://doi.org/10.1017/S002211209800127X.
Miquel, A.M., Kamath, A., Chella, M.A., Archetti, R., Bihs, H., 2018. Analysis of different methods for wave generation and absorption in a CFD-based numerical wave tank. J. Mar. Sci. Eng. https://doi.org/10.3390/jmse6020073.
Ramirez, C., Renouard, D., 1998. Generation of internal waves over a shelf. Dynam. Atmos. Oceans. https://doi.org/10.1016/S0377-0265(98)00048-7.
Si, Z., Zhang, Y., Fan, Z., 2012. A numerical simulation of shear forces and torques exerted by large-amplitude internal solitary waves on a rigid pile in South China Sea. Appl. Ocean Res. https://doi.org/10.1016/j.apor.2012.05.002.
Song, Z.J., et al., 2011. Comparisons of internal solitary wave and surface wave actions on marine structures and their responses. Appl. Ocean Res. https://doi.org/10.1016/j.apor.2011.01.003.
Vázquez, A., Bruno, M., Izquierdo, A., Macías, D., Ruiz-Cañavate, A., 2008. Meteorologically forced subinertial flows and internal wave generation at the main sill of the Strait of Gibraltar. Deep. Res. Part I Oceanogr. Res. Pap. https://doi.org/10.1016/j.dsr.2008.05.008.
Xu, Z., Yin, B., Hou, Y., Fan, Z., Liu, A.K., 2010. A study of internal solitary waves observed on the continental shelf in the northwestern South China Sea. Acta Oceanol. Sin. https://doi.org/10.1007/s13131-010-0033-z.
Yan, H., Zhang, F., Yu, J., 2016. The Lectotype Optimization Study on Submerged Floating Tunnel Based Delphi Method. https://doi.org/10.1016/j.proeng.2016.11.574.
Zhu, H., Wang, L., Avital, E.J., Tang, H., Williams, J.J.R., 2016. Numerical simulation of interaction between internal solitary waves and submerged ridges. Appl. Ocean Res. 58 https://doi.org/10.1016/j.apor.2016.03.017.
Zou, P.X., Bricker, J.D., Uijttewaal, W.S.J., 2020a. Impacts of extreme events on hydrodynamic characteristics of a submerged floating tunnel. Ocean Eng. 218 https://doi.org/10.1016/j.oceaneng.2020.108221.
Zou, P., Bricker, J., Uijttewaal, W., 2020b. Optimization of submerged floating tunnel cross section based on parametric Bézier curves and hybrid backpropagation - genetic algorithm. Mar. Struct. https://doi.org/10.1016/j.marstruc.2020.102807.
Zou, P.X., Bricker, J.D., Uijttewaal, W., 2020c. A Parametric Method for Submerged Floating Tunnel Cross-Section Design, 2020, The 30th International Ocean and Polar Engineering Conference.
Zou, P.X., Bricker, J.D., Uijttewaal, W.S.J., 2020d. Submerged floating tunnel cross-section analysis using a transition turbulence model. J. Hydraul. Res. https://doi.org/10.1080/00221686.2021.1944921.
Zou, P.X., Bricker, J.D., Chen, L.Z., Uijttewaal, W., Ferreira, C.S., 2021. Response of a submerged floating tunnel subject to flow-induced vibration. J. Eng. Struct. Submitted for publication.